


Fock-state-lattice approach to quantum optics

Pil Saugmann and Jonas Larson

Department of Physics, Stockholm University, AlbaNova University Center, 106 91 Stockholm, Sweden (Received 6 May 2022; revised 6 November 2022; accepted 17 January 2023; published 28 September 2023)

We analyze a set of models frequently appearing in quantum optical settings by expressing their Hamiltonians in terms of Fock-state lattices (FSLs). The few degrees-of-freedom of such models, together with the system symmetries, make the emerging FSLs relatively simple such that they can be linked to known lattice models from the condensed-matter community. Thus, the FSLs may shed new light on known quantum optical systems. While we provide a rather long list of models and their corresponding FSLs, we pick a few to demonstrate the method's strength. The three-mode boson model, for example, is shown to display a fractal spectrum and chiral evolution in the FSL characterized by localized distributions traversing along symmetric trajectories. In a second example, we consider the central spin model, which generates an FSL reminiscent of the Su-Schrieffer-Heeger model hosting topological edge states. We further demonstrate how the phenomenon of flat bands in lattice models can manifest in related FSLs, which can be linked to so-called dark states.

DOI: [10.1103/PhysRevA.108.033721](https://doi.org/10.1103/PhysRevA.108.033721)**I. INTRODUCTION**

Lattice models often serve as a powerful tool for investigating condensed-matter systems [1]. They arise naturally in many situations, most notably in crystal structures. At the same time, they provide a direct link to computational physics as all continuous models turn into lattice models when discretized. In the realm of quantum simulators, lattice models have come to play a central role, as, for example, in the pioneering cold-atom experiments demonstrating the realization of a Bose-Hubbard-model [2]. These are many-body interacting models that often cannot be analytically solved in contrast to quadratic models. Recently, it was shown that quadratic bosonic models with only a few degrees-of-freedom can be mapped to lattice spin models exhibiting interesting topological features [3]. Going beyond quadratic models, the aforementioned reference can be seen as proposing a direction in which also unsolvable lattice models can be studied. Generally, properties of lattice models typically rely on the lattice symmetries and their dimensions and not on the physical realization, e.g., topological features may survive breaking of translational symmetry. This motivates us to look for novel ways to realize well-known and new lattice models, which, in the long run, could potentially also pave the way to solving computational hard problems.

Traditionally, the geometry of the lattice is rooted in the system's spatial dimensions, i.e., we consider lattices in three or lower dimensions. There are no such limitations

in mathematics. Synthetic lattice dimensions occur in various proposals for quantum simulators as a route toward new exotic models [4–7]. Examples of this are utilizing atomic internal degrees-of-freedom [4], or vibrational states of the harmonic trapping potential [5], which can be employed to create synthetic dimensions for ultracold atoms loaded in optical lattices. More generally, if we give up the idea of a lattice living in real space, any Hamiltonian \hat{H} , single-particle or many-body, can be described as a single-particle system if mapped into state space. In such a view, a latticelike structure emerges by identifying the different basis states with the lattice sites. Then, \hat{H} is a matrix in which the diagonal terms serve as on-site energies in the lattice, and the off-diagonal elements give the tunneling rates between these sites. Typically, such a lattice will rapidly grow in complexity as the number of degrees-of-freedom is increased, and it might be that not much new insight is gained by such a viewpoint.

Furthermore, we will require that the chosen basis should be physically relevant. Paradigmatic light-matter models in quantum optics seem perfect; it is possible to isolate a few appropriate degrees-of-freedom, and the natural basis comprises the bare Fock states. Hence, their Hamiltonians give rise to manageable Fock-state lattices (FSLs). The FSL emerging from the Jaynes-Cummings (JC) model was already introduced in Ref. [8], and it was studied further in Ref. [9] to explore a new type of topological matter formed by quantized light. We note that, historically, similar lattice ideas have been discussed in terms of so-called Glauber-Fock lattices in waveguide systems of classical light [7].

In this work, we bring forward several light-matter type models, although we focus on just a few of them. It turns out that these capture the general ideas, at the same time as the physics is extremely rich despite their simplicity. Taking the multimode JC model as an example, in the high detuned limit, the spin degree-of-freedom freezes out, and one

Published by the American Physical Society under the terms of the Creative Commons Attribution 4.0 International license. Further distribution of this work must maintain attribution to the author(s) and the published article's title, journal citation, and DOI. Funded by Bibsam.

reaches an effective quadratic Hamiltonian consisting only of bosonic degrees-of-freedom. The Fock states provide a natural basis to study such systems, and the sparseness of the Hamiltonian makes the FSLs convenient for getting insight into the models. For three bosonic modes, a triangular FSL emerges, and by further imposing a synthetic magnetic flux, the system's spectrum becomes fractal, akin to the Hofstadter butterfly spectrum of two-dimensional (2D) tight-binding lattice models exposed to homogeneous perpendicular magnetic fluxes [10]. However, the FSLs studied in this paper lack translational invariance; hence, the fractal structure is not derived from the same mechanism as for the Hofstadter models. The properties of our fractal spectrum imply that initial Fock states will follow symmetric curves within the FSL. As another example, we consider the central spin model in which a single spin-1/2 particle interacts identically with N other spin-1/2 particles. By tuning the interaction, it is possible to create an FSL similar to the Su-Schrieffer-Heeger (SSH) model. As for the SSH model, one finds exponentially localized edge states. Related to this, we also discuss a few models that support a large number of degenerate $E = 0$ eigenstates, which serve as the counterpart of flat bands such as, for example, Lieb lattices.

The structure of the paper is as follows. In the next section, we systematically introduce the FSLs. First, they are introduced for the resonant JC models, and from there, we elaborate on how one may design interesting FSLs by looking at related models. In Sec. III we discuss the role of underlying symmetries. In Sec. IV, multimode JC models in the large detuned limit are considered when a synthetic flux has been included. For these systems, we see how a fractal-like structure of the energy spectrum appears for certain fluxes, which motivates us to study in Sec. V how initially localized states evolve within the FSL. Section VI discusses a connection between the central spin model and the SSH model, namely the appearance of exponentially localized edge states in the FSL. Finally, in Sec. VIII we summarize our findings.

II. RESONANT JAYNES-CUMMINGS MODELS AND THEIR FOCK-STATE LATTICES

A. Multimode Jaynes-Cummings models

In this section we introduce the JC model, which, as the simplest example of a spin-boson model, will serve as a starting point for building other models with interesting underlying FSLs. The JC model, first introduced by Jaynes and Cummings in 1963 [11], provides a fully quantum-mechanical treatment of an atom interacting with an electromagnetic field [12]. The original model consists of a two-level atom, pseudo-spin-1/2 particle, interacting with a single bosonic mode representing the electromagnetic field. The interaction can be understood as an exchange of excitations between the atom and the field; when the ground state is excited to the excited state, the number of bosons is lowered by 1, and vice versa for deexcitation to the ground state. This gives rise to a Hamiltonian of the form

$$\hat{H}_{\text{JC}} = \hat{H}_0 + \hat{H}_{\text{int}}, \quad (1)$$

with the noninteracting, or bare, part of the Hamiltonian \hat{H}_0 comprising the free energies of the field and atom, i.e.,

$$\hat{H}_0 = \omega \hat{n} + \frac{\Omega}{2} \hat{\sigma}^z, \quad (2)$$

where we have set $\hbar = 1$, ω is the photon frequency, and Ω is the transition frequency for the two-level atom. Further, for the boson number operator $\hat{n}|n\rangle = n|n\rangle$ for some Fock state $|n\rangle$, and $\hat{\sigma}^z$ is the Pauli z -matrix, which upon acting on the bare atomic states $\hat{\sigma}^z|g\rangle = -|g\rangle$ and $\hat{\sigma}^z|e\rangle = |e\rangle$, with $|g\rangle$ and $|e\rangle$ the lower and upper atomic states, respectively. Following the logic of bosonic states, we will also refer to the atomic basis states, such as $|g\rangle$ and $|e\rangle$, as Fock states. Returning to the interaction part \hat{H}_{int} , both the atom and the bosonic mode emit and absorb excitations, and we may write the interaction Hamiltonian as [12]

$$\hat{H}_{\text{int}} = g(\hat{\sigma}^+ + \hat{\sigma}^-)(\hat{a} + \hat{a}^\dagger), \quad (3)$$

with g the light-matter interaction strength. It includes four different contributions, two of which preserve the number of excitations in the system and two corresponding to simultaneous excitation/deexcitation of the two degrees-of-freedom. The latter do not conserve the bare energy of the system, and for now, we shall drop them both. This approximation is what is called the rotating-wave approximation (RWA), and it leads to an interaction of the form [12]

$$\hat{H}_{\text{int}} = g(\hat{a}^\dagger \hat{\sigma}^- + \hat{\sigma}^+ \hat{a}). \quad (4)$$

Moving to the interaction picture with respect to $\omega \hat{N}$, with $\hat{N} = \hat{n} + \frac{1}{2} \hat{\sigma}^z$ the excitation number operator, the number of free parameters can be reduced from three to two. Defining the atom-field detuning as $\Delta = \Omega - \omega$, the Hamiltonian (in this interaction picture) can be written as

$$\hat{H}_{\text{JC}} = \frac{\Delta}{2} \hat{\sigma}^z + g(\hat{a}^\dagger \hat{\sigma}^- + \hat{\sigma}^+ \hat{a}), \quad (5)$$

which is the celebrated JC Hamiltonian.

The JC model can be expanded in numerous ways, of which the most common ones are [12] *multimodes*, where more than one boson mode is considered; a *multilevel atom*, in which more than two electronic levels couple to the electromagnetic field; a *multiatom*, where N identical two-level atoms couple to the boson mode (the so called Dicke model); or *pumped/driven* models. Focusing on the first extension for now (and returning to the other below), and labeling each boson mode by an index i and assuming that the atom couples to each bosonic mode with a corresponding coupling strength g_i , the multimode JC model takes the form

$$\hat{H} = \frac{\Omega}{2} \hat{\sigma}^z + \sum_i \omega_i \hat{n}_i + \sum_i g_i (\hat{\sigma}^+ \hat{a}_i + \hat{\sigma}^- \hat{a}_i^\dagger). \quad (6)$$

As for the regular JC model, we could turn to an interaction picture with respect to the total excitation number, which is especially convenient in the degenerate case when $\omega_i \equiv \omega, \forall i$.

B. Fock-state lattices for the resonant multimode Jaynes-Cummings models

From the single-mode JC model, we first see how the latticelike structure emerges in state space. As long as the

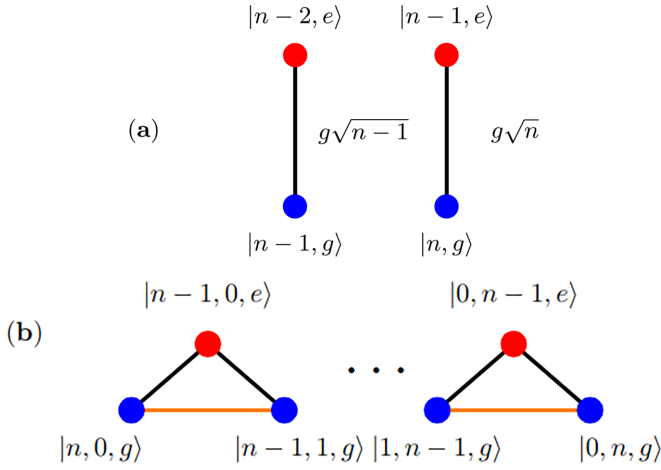


FIG. 1. The FSL for the single-mode JC (a) and two-mode JC (b) models, with red (blue) dots marking the atomic $|e\rangle$ ($|g\rangle$) states, note that for two modes, the FSL is a fully connected triangular chain. One finds an infinite series of two-site lattices in the former, and in the latter one has a 1D chain. The black lines indicate the nonzero tunnelings of the lattice in the resonant limit, whereas the orange lines (in the two-mode model) are the same but in the large detuned limit when the excited atomic level $|e\rangle$ has been adiabatically eliminated. In both cases, the tunneling rates scale such that the lattice is not translationally invariant ($\sqrt{n_i}$ in the resonant case, black lines; and $\sqrt{n_a n_b}$ in the large detuning limit, orange lines).

coupling $g \neq 0$, the Fock states are generally not the eigenstates of the JC model; instead, they provide a natural basis for analyzing the system's dynamics. Consider first the Fock states for the single-mode JC model, $|n, e\rangle$ and $|n, g\rangle$. Letting the Hamiltonian in (5) act on these states, one finds that, except for the vacuum state, they will couple pairwise as

$$|n, g\rangle \longleftrightarrow |n-1, e\rangle. \quad (7)$$

Thus, the JC Hamiltonian is 2×2 block diagonal in the Fock basis.

It is important to appreciate that the Fock states are coupled by the interaction Hamiltonian (4) alone, while the bare part \hat{H}_0 of the Hamiltonian acts only as on-site energy shifts in the FSL. Throughout this paper, we break up the Hamiltonian of the problem as $\hat{H} = \hat{H}_0 + \hat{H}_{\text{int}}$, where the first part only contributes to on-site energy shifts but not any kinematics, which instead is contained within the interacting part \hat{H}_{int} . Indeed, the lattice geometry and its tunneling rates are defined via \hat{H}_{int} , and we will thereby focus on the lattices deriving from the interaction Hamiltonians without paying any attention to the energy shifts. On some occasions, the bare part will only contribute to an overall energy shift, while its role is more complicated in others. In such cases, we imagine working in an interaction picture.

Returning to the JC model, the Hamiltonian decouples into blocks, and the related lattice structure becomes rather trivial, as shown in Fig. 1(a). We find an infinite set of two-site lattices; alternatively, we find a ladder lattice with zero tunneling rates along the legs. One should note that as $\hat{a}^\dagger |n\rangle = \sqrt{n} |n+1\rangle$, the tunneling rate scales with \sqrt{n} for the two-site lattice n . This property is general for all our models, i.e., the tunnelings are not constant throughout the lattices, hence the

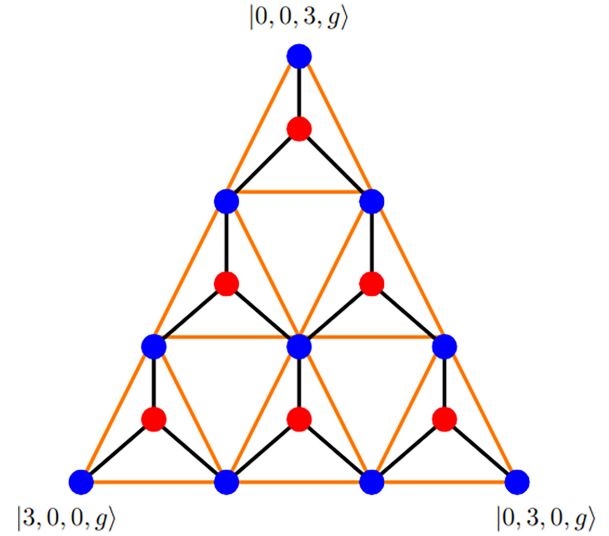


FIG. 2. Same as for Fig. 1 but for the three-mode JC model. Here we show it for the $N = 3$ excitation sector, which results in a finite lattice comprising 16 sites (increasing N makes the lattice larger). In the resonant case, the FSL forms a hexagonal structure in which each site couples to three neighbors (envisioned by the solid black lines). At the same time, in the detuned limit, one of the atomic states (red or blue dots) is adiabatically eliminated, and a triangular FSL is derived, where every site couples to six neighboring sites instead (shown by the solid orange lines).

lattices do not possess translational invariance. A consequence is that Bloch's theorem does not apply, and we typically find a point spectrum rather than a band spectrum.

For the two-mode JC model, a similar, but still conceptually different, picture arises. The interaction Hamiltonian in Eq. (6) reduces to

$$\hat{H}_{\text{int}} = (g_A \hat{\sigma}^+ \hat{a} + g_B \hat{\sigma}^+ \hat{b} + \text{H.c.}). \quad (8)$$

As there are now two boson modes, the Fock states will take the form $|n_A, n_B, g\rangle$ and $|n_A, n_B, e\rangle$. According to Eq. (8), the states couple as

$$\dots |n_A, n_B - 1, e\rangle \leftrightarrow |n_A, n_B, g\rangle \leftrightarrow |n_A - 1, n_B, e\rangle \dots \quad (9)$$

Hence, for the two-mode JC model, a latticelike structure of two identical copies of 1D chains results; see Fig. 1(b). As for the single-mode JC model, the couplings scale with \sqrt{n} . In the two-mode JC model, the atom can mediate photon transfer between the two modes [12], which for the FSL implies moving left or right along the 1D lattice.

Finally, we consider the FSL for the three-mode JC model, which was first introduced in Ref. [8]. For a single mode, there is only a single neighboring state to tunnel to [see Eq. (7)], while for two modes there are two neighboring states, and we then build up a 1D chain. For three modes, a , b , and c , we have three neighboring sites, and as such, the resulting lattice will be hexagonal, as shown in Fig. 2. The hexagonal lattice has a sublattice triangular structure seen as the red and blue dots in the figure, which further represent the different atomic states; $|g\rangle$ (blue) and $|e\rangle$ (red). These triangular sublattices will be those surviving in the large detuning limit, as shown in the next section. The translationally invariant hexagonal lattice

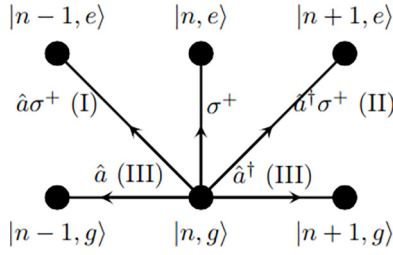


FIG. 3. Schematic representation of the zeroth- and first-order couplings of Fock states. The order of the coupling refers to the number of participating boson creation or annihilation operators in each tunneling process.

has several interesting features [13], e.g., the presence of Dirac cones at the corners of the Brillouin zone. Furthermore, if tunneling beyond the nearest neighbor is considered (the Haldane model), the model may host topological features, which were analyzed for the FSL in [9]. One could generalize this construction of the FSLs to the n -mode JC model, resulting in a lattice in an $(n - 1)$ -dimensional space.

C. Beyond the rotating-wave equation— The quantum Rabi model

Returning to the Hamiltonian of Eq. (3), we are immediately presented with another lattice model if we keep the counter-rotating terms rather than dismiss them. This model is called the quantum Rabi model [12,14]. More compactly, the interaction Hamiltonian can be expressed as $\hat{H}_{\text{int}} = g(\hat{a}^\dagger + \hat{a})\hat{\sigma}_x$, where $\hat{\sigma}_x$ is the Pauli- x matrix; $\hat{\sigma}_x|g(e)\rangle = |e(g)\rangle$. This Hamiltonian does not preserve the number of excitations as the JC Hamiltonian of Eq. (5). The counter-rotating terms break down the continuous symmetry of the JC model to a discrete \mathbb{Z}_2 -parity symmetry [14]. We will discuss the role of symmetries in more general terms below. For the FSL, these terms change the number of excitations by 1, i.e., they connect the 2×2 blocks of the JC Hamiltonian. In addition, each Fock state now couples to two neighboring Fock states,

$$\dots |e, -2\rangle \longleftrightarrow |g, n-1\rangle \longleftrightarrow |e, n\rangle \longleftrightarrow |g, n+1\rangle \dots \quad (10)$$

With two neighbors, the FSL becomes a 1D chain (see Fig. 4). The aforementioned \mathbb{Z}_2 -symmetry implies two decoupled parity sectors, meaning that we actually get two copies of the chain. If we consider the anisotropic quantum Rabi model [15], we have that the counter-rotating terms couple with a different coupling amplitude than the excitation-preserving terms, i.e., the interaction Hamiltonian takes the form

$$\hat{H}_{\text{int}} = g_{\text{jc}}(\hat{\sigma}_+\hat{a} + \hat{a}^\dagger\hat{\sigma}_-) + g_{\text{ajc}}(\hat{\sigma}_-\hat{a} + \hat{a}^\dagger\hat{\sigma}_+). \quad (11)$$

This difference does not change the lattice geometry, but an alternation between the tunneling rates of every second site occurs. For a translationally invariant system, this would mean that the lattice had a bipartite structure where every unit cell would consist of two sites. This model is the well-known Su-Schrieffer-Heeger (SSH) model [13,16], which has exponentially localized topologically protected zero-energy edge

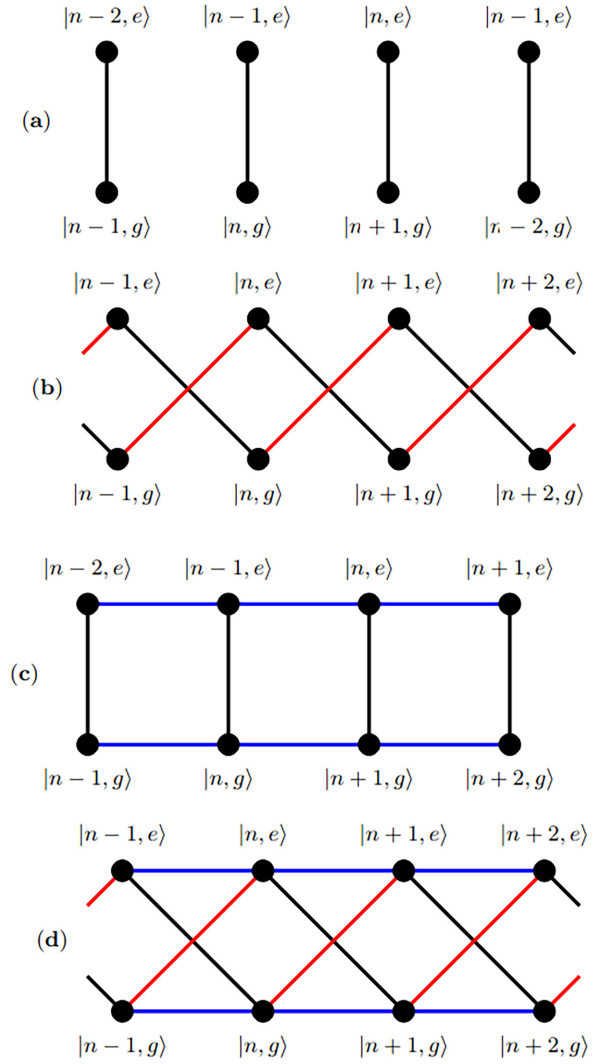


FIG. 4. Summary of FSLs for models consisting of only a single boson and two-level atomic degree-of-freedom. In (a), the lattice of the JC model (4) is shown. Here, the conservation of \hat{N} reduces the dimension of the system such that an infinite set of two-site lattices emerges. The second plot (b) gives the FSL for the quantum Rabi model (11), with red lines marking the tunneling due to the counter-rotating terms, and the black lines showing the JC interaction terms. Note that these are two copies of 1D chains, even though they are drawn in this zigzag way. The FSL of the driven JC model is shown in (c). The blue lines mark the tunneling stemming from the driving, i.e., by removing them, we return to the JC lattice (a). Finally, in (d), we display the FSL of the driven quantum Rabi model [again, the lattice in (b) is regained by omitting the blue lines]. This lattice is similar to a Creutz lattice with known interesting properties (see the main text). A drive of the spin instead of the boson would result in vertical blue lines rather than horizontal ones.

states. Similar edge states are also found in the anisotropic quantum Rabi model. However, an obstacle here is that the FSL of the anisotropic quantum Rabi model has only one and not two edges (the boson Fock space has no upper bound). Furthermore, even though the edge state is localized to the edge, it is not exponentially localized. However, one can introduce another model supporting a finite FSL, which we do

in Sec. VI, in which the edge states come out more natural and are exponentially localized.

The above demonstrates how the different coupling terms manifest as tunneling rates in the FSL. We shall explore this systematically to construct other FLSs. In Fig. 3 the three different couplings of a Fock state consisting of a single boson mode and a spin half excitation are shown. We label the couplings (*I*) – (*III*), and refer to them as first-order couplings since they all consist of a single-boson creation or annihilation operator and, therefore, all scale with \sqrt{n} . The last coupling is shown in Fig. 3 and only comprises a coupling of the spin mode—and no boson operator—and is, therefore, a zeroth-order coupling. We do not consider the purely spin coupling any further; higher-order couplings typically lead to couplings beyond nearest neighbors and may lead to a new interesting latticelike structure. The (*I*) term is the JC coupling, and the (*II*) is the counter-rotating coupling, which we have already discussed. The last couplings, marked by (*III*), stem from driving the boson mode. Including the drive term is discussed for the JC model in the section below, and for the quantum Rabi model it is discussed in Sec. II.

D. Driven Jaynes-Cummings-like systems

As mentioned above, the counter-rotating terms lower the symmetry of the JC model, and the 2×2 block structure of the Hamiltonian in the Fock basis is lost. Looking at the JC FSL in Fig. 1(a), this implies additional coupling terms such that we find two 1D chains, one for each parity. We can break the continuous $U(1)$ number conservation symmetry in several ways. A natural way to break this symmetry is to consider the driven JC model, where we include a field drive

$$\hat{H}_{\text{fd}} = \eta(\hat{a} + \hat{a}^\dagger), \quad (12)$$

or an atom drive

$$\hat{H}_{\text{ad}} = \eta\hat{\sigma}_x. \quad (13)$$

The excitation number is no longer preserved for either of these, while both still support a \mathbb{Z}_2 -parity symmetry. More precisely, the field drive causes nonzero horizontal tunneling in the FSL of Fig. 1(a), and the atom drive results in diagonal tunneling terms. As for the anisotropic quantum Rabi model, which mimicked the SSH model with broken translational invariance, the driven quantum Rabi model realizes a Creutz ladder [17] with broken translational invariance; see Fig. 4(d). The Creutz ladder has attracted attention as it may host dispersionless, i.e., flat bands. Naturally, such flat bands do not occur in the driven quantum Rabi model since it is no longer translationally invariant. However, remnants of these bands are still present. For field driving, the interaction Hamiltonian (after a rotation $\hat{\sigma}_x \rightarrow \hat{\sigma}_z$) can be written as

$$\hat{H}_{\text{int}} = (\eta + g\hat{\sigma}_z)(\hat{a} + \hat{a}^\dagger), \quad (14)$$

which results in two energy branches for which one is flat provided $\eta = \pm g$. However, this is only true in the interaction picture; the bare Hamiltonian \hat{H}_0 would lift this degeneracy and cause the Hamiltonian to be bounded from below.

III. NOTE ON SYMMETRIES AND LATTICE DIMENSIONS

We have seen a couple of examples in which the structure, especially the lattice's dimensionality, changes if the system's symmetry is altered. Here we give some general rules for how this comes about.

Returning to Fig. 3, we may also use it to prove a recipe for how one may construct even more elaborate FSLs. First, this figure considers a system of a single-boson mode and a two-level atom. However, we could expand it to multilevel atoms, several boson modes, or a combination of these. Suppose we replace the spin-1/2 atom with an atom with spin S . In that case, it will provide a pseudodimension of $2S + 1$ sites depth, while including another boson mode adds an extra dimension (infinitely deep). Generally, the bosonic modes, constituting one continuous degree-of-freedom, give rise to one lattice dimension, such that with each additional bosonic mode, the dimension of the FSL grows with one. The atom, which provides a discrete degree-of-freedom, causes an extra lattice pseudodimension, i.e., the lattice is finite in the new dimension.

A continuous $U(1)$ symmetry reduces the lattice dimension by unity, while a discrete \mathbb{Z}_n symmetry decouples the lattice into sublattices. For example, as the JC model consists of one continuous boson degree-of-freedom and a discrete atomic degree-of-freedom, one might expect a ladder with two legs. However, number conservation reduces the lattice dimension by one, prohibiting tunneling along the ladder's legs. On the other hand, the quantum Rabi model does not support particle conservation, and we allow tunneling along the legs. At the same time, the parity symmetry causes the rung tunnelings to be zero. Further, a continuous symmetry can make the size of the lattice finite, apart from reducing the dimension. Examples of these are given in Sec. IV.

Given some Hamiltonian, its FSL typically supports some discrete point symmetries. Take for example the triangular FSL of Fig. 2, which clearly has a $2\pi/3$ rotational symmetry around its center site, and three mirror reflections. These lattice symmetries can be traced back to symmetries of the Hamiltonian, e.g., the rotational symmetry translates to the unitary transformation

$$\hat{a} \rightarrow \hat{b}, \hat{b} \rightarrow \hat{c} \quad \text{and} \quad \hat{c} \rightarrow \hat{a}. \quad (15)$$

The lattice geometry, e.g., the number of neighbors, is determined by the specific form of the interaction Hamiltonian. When expressed in terms of raising/lowering operators (e.g., \hat{a} and $\hat{\sigma}^-$), the number of terms in \hat{H}_{int} gives the maximum number of possible neighbors. There are four terms in the quantum Rabi model, but only two cause coupling to other states since $\hat{\sigma}^+ |e\rangle = \hat{\sigma}^- |g\rangle = 0$. The interaction terms may represent tunneling either between nearest neighbors in the FSL or beyond, like for the Creutz ladder as shown in Fig. 4(d).

IV. THE LARGE DETUNING LIMIT—QUADRATIC BOSONIC MODELS

A. Effective bosonic models

Quadratic spin-boson models are intrinsically nonlinear due to the finite spin Hilbert spaces. However, there is a

natural regime in which the models become approximately linear, namely in the large detuning limit. Here we assume $|\Delta| \gg g\sqrt{n}$. The fast timescale is set by Δ , and we face the situation where the atomic degree-of-freedom follows that of the boson. Hence, it is enough to consider the evolution of the bosons. The effective Hamiltonian that dictates the bosonic dynamics can be derived by adiabatic elimination [18]. Here one first writes down the Heisenberg equations for both the boson and spin operators, which for the JC model read

$$\begin{aligned}\partial_t \hat{a} &= -i[\hat{a}, \hat{H}_{\text{JC}}] = -ig\hat{\sigma}^-, \\ \partial_t \hat{\sigma}^- &= -i\Delta\hat{\sigma}^- + ig\hat{a}\hat{\sigma}_z, \\ \partial_t \hat{\sigma}_z &= 2ig(\hat{a}^\dagger \hat{\sigma}^-).\end{aligned}\quad (16)$$

As the fast timescale is set by Δ^{-1} , the spin operators can be replaced by their steady-state solutions, i.e., $\hat{\sigma}^- = \frac{g}{\Delta}\hat{a}\hat{\sigma}_z$, and after inserting this into the first equation above, the effective dynamical equation for \hat{a} becomes

$$\partial_t \hat{a} = -\frac{g^2}{\Delta}\hat{a}\hat{\sigma}_z \equiv -i[\hat{a}, \hat{H}_{\text{eff}}], \quad (17)$$

where in the second step we define the effective bosonic Hamiltonian \hat{H}_{eff} . Solving this operator equation gives

$$\hat{H}_{\text{eff}} = \frac{2g^2}{\Delta}\hat{n}\hat{\sigma}_z. \quad (18)$$

In the case of more than one boson mode, the adiabatic elimination is straightforward to generalize. With the summation over an index i on the bosonic operator, the effective Hamiltonian stays the same such that

$$\begin{aligned}\partial_t \hat{a}_i &= -ig_i\hat{\sigma}^-, \\ \partial_t \hat{\sigma}^- &= -i\Delta\hat{\sigma}^- + i\sum_i g_i\hat{a}_i\hat{\sigma}_z, \\ \partial_t \hat{\sigma}_z &= 2i\sum_i g_i\hat{a}_i^\dagger\hat{\sigma}^-.\end{aligned}\quad (19)$$

Hence, with $\partial_t \hat{\sigma}^- = 0$ we obtain $\hat{\sigma}^- = \sum_i \frac{g_i\hat{a}_i\hat{\sigma}_z}{\Delta}$ such that

$$\hat{H}_{\text{eff}} = \sum_{i \neq j} \frac{2g_i g_j}{\Delta} \hat{a}_i^\dagger \hat{a}_j \hat{\sigma}_z. \quad (20)$$

From a perturbative perspective, the effective Hamiltonians describe the virtual processes of absorbing and emitting a photon—the Stark shift. In the multimode case, such two-photon processes act as beam-splitters among the involved modes such that bosons will tunnel from one mode to another. This manifests as nonvanishing tunneling rates in the corresponding FSLs.

B. Fock state lattices for multimode JC models in the large detuning limit

We set out to study their properties with the effective Hamiltonian in Eq. (20). Noting that in the detuned limit no population is transferred between the atomic states, the spin part of the Fock state becomes trivial, and we can leave it out for now. Generally, the interaction Hamiltonian for the detuned multimode case can be written in the form

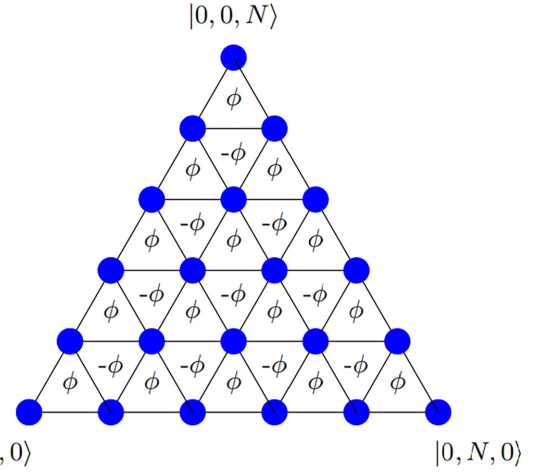


FIG. 5. The triangular FSL derived from the three-mode boson model (21). A synthetic magnetic flux $\pm\phi$ penetrates each plaquette in a staggered manner. The corner states are represented by the Fock states with two modes in vacuum. Along the straight lines, two diagonal and one horizontal, the boson number is fixed in one of the modes, e.g., for the horizontal lines the third c -mode keeps a fixed particle number. These observations hold for higher-dimensional lattices as well—in the four-mode model, one finds a tetrahedral lattice.

$\hat{H}_{\text{int}} = \sum_{i \neq j} \tau_{ij} \hat{a}_i^\dagger \hat{a}_j$. This Hamiltonian describes noninteracting bosons living on a lattice defined by the subscripts i and j , e.g., for two and three modes we get a bosonic “dimer” or “trimer,” respectively. However, we are interested in their respective FSLs. *A priori*, the tunneling strengths τ_{ij} depend on the system details. For degenerate modes and appropriate polarizations, it is natural to assume that they all have the same amplitudes, i.e., $\tau_{ij} = \tau e^{i\phi_{ij}}$. The phases ϕ_{ij} can, in principle, be experimentally controlled [9]. We include these phases since we will see that their presence leads to many interesting phenomena. Taking this into account, we reach the final Hamiltonian

$$\hat{H}_{\text{int}} = \tau \sum_{i \neq j} e^{i\phi_{ij}} \hat{a}_i^\dagger \hat{a}_j. \quad (21)$$

Note that hermiticity implies that $\phi_{ij} = -\phi_{ji}$, and since the tunneling rate only sets the timescale, we pick $\tau = 1$ throughout. For two modes (label them with a and b) this Hamiltonian reduces to $\hat{H}_{\text{int}} = (e^{i\phi} \hat{a}^\dagger \hat{b} + e^{-i\phi} \hat{b}^\dagger \hat{a})$ in which the phase can be trivially omitted by a gauge transformation. However, this will not be true in general [19] for three or more modes. The phases will result in complex tunneling rates in the FSLs. According to the idea of the Peierls substitution, these phases mimic a synthetic magnetic flux penetrating the lattice perpendicularly [13]. If a loop in the lattice is formed, the (gauge-invariant) magnetic flux ϕ through the loop equals the sum of the phases of the corresponding tunneling rates. Typically we are interested in the smallest such loop, a lattice plaquette, and its corresponding flux; see Fig. 5. Consider, for example, three boson modes a , b , and c . From Eq. (21) we have the three phases ϕ_{ab} , ϕ_{bc} , and ϕ_{ca} . Each of these can be changed via a gauge transformation, but the sum $\phi = \phi_{ab} + \phi_{bc} + \phi_{ca}$ remains constant under such transformations. The corresponding FSL is a triangular lattice with a staggered

magnetic flux, i.e., alternating $\pm\phi$ fluxes through each triangular plaquette; see Fig. 5. If we choose that $\phi_{ij} = \phi$ for any $i < j$, then for all higher-dimensional multimode FSLs, the same pattern will emerge, i.e., any 2D plane/cut of the FSL will display a triangular lattice with a staggered $\pm\phi$ field. We may note in passing that it is possible to also have a homogeneous field in the FSL. However, it turns out that this is only possible for nonquadratic boson models, i.e., interacting many-body systems [20].

As the Hamiltonian in Eq. (21) preserves the number of particles, there is a corresponding $U(1)$ -symmetry. This symmetry lowers the lattice dimension by 1, e.g., the three-mode model generates a 2D FSL, and so on. Generally, for any number of modes, the unit cell has the form of a d -simplex, where d indicates the number of dimensions, e.g., in 2D it is a triangle, in 3D it is a tetrahedron, and so on. However, it should be stressed that in a strict sense, we do not have unit cells since the lattice is not translationally invariant, but here we think only of the lattice geometry. Furthermore, the lattice is finite for a given particle number N , with the corners represented by the Fock states with all N bosons occupying a single mode and the remaining ones in a vacuum. For example, for three modes with N bosons, the number of sites of the FSL becomes $S = (N + 1)(N + 2)/2$. Finally, we note that introducing a synthetic field breaks time-reversal symmetry. However, for $\phi = \pi/2$ the spectrum becomes symmetric around $E = 0$, which is a manifestation of a chiral symmetry given by the unitary $\hat{U}_C = \hat{K} \exp(i\pi \hat{n}_c)$, where \hat{K} stands for complex conjugation, which anticommutes with the Hamiltonian.

C. Closer look at the three-mode model—A fractal spectrum

In this section, we limit ourselves to the three-mode model with a varying flux. Later we comment also on higher-dimensional models. In particular, we are interested in the energy spectrum for the Hamiltonian given in Eq. (21) as a function of the flux ϕ . The translationally invariant case of a 2D lattice exposed to a constant perpendicular magnetic field results in a fractal spectrum known as the Hofstadter butterfly [10]. It is relevant to analyze similar situations for the FSLs. For this objective we use that the Hamiltonian is quadratic and can be written as $\hat{H}_{\text{int}} = \hat{\mathbf{a}}^\dagger h \hat{\mathbf{a}}$, where

$$h = \begin{bmatrix} 0 & e^{i\phi} & e^{i\phi} \\ e^{-i\phi} & 0 & e^{i\phi} \\ e^{-i\phi} & e^{-i\phi} & 0 \end{bmatrix} \quad (22)$$

and $\hat{\mathbf{a}}^\dagger = (\hat{a}^\dagger, \hat{b}^\dagger, \hat{c}^\dagger)$. If we diagonalize h , i.e., $d = UhU^{-1}$, the full Hamiltonian is diagonalized as $\hat{H}_{\text{int}} = \gamma_0 \hat{\alpha}_0^\dagger \hat{\alpha}_0 + \gamma_1 \hat{\alpha}_1^\dagger \hat{\alpha}_1 + \gamma_2 \hat{\alpha}_2^\dagger \hat{\alpha}_2$, with $\hat{\alpha}_k$ ($k = 0, 1, 2$) the transformed boson operators, and γ_k the eigenvalues of h . Thus, the spectrum for a single boson is simply the eigenvalues of h , while the full spectrum, given N bosons, can be found combinatorically from these single-boson energies γ_k . We may note that the structure of h in Eq. (22) remains for higher dimensions. Numerically its eigenvalues can be found for large mode numbers, but analytical solutions are only found for the three- and four-mode cases. For the three-mode model, finding the single-boson energies reduces to solving the characteristic polynomial $\gamma^3 - 3\gamma - 2 \cos \phi = 0$, which leads to the three

energies

$$\gamma_k = 2 \cos \left(\frac{\phi - 2 \times \pi \times k}{3} \right), \quad k \in \{0, 1, 2\}. \quad (23)$$

Hence, the full spectrum for a general boson number is written as

$$E_{\mathbf{n}} = n_0 \gamma_0 + n_1 \gamma_1 + n_2 \gamma_2, \quad (24)$$

where $\mathbf{n} = (n_0, n_1, n_2)$ subject to the constraint $n_0 + n_1 + n_2 = N$. To gain further insight into the spectral structure, we consider the energy differences between any two energy levels,

$$\delta E_{\mathbf{n}} = E_{\mathbf{n}} - E_{\tilde{\mathbf{n}}} = (\gamma_1 - \gamma_0)(n_1 - \tilde{n}_1) + (\gamma_2 - \gamma_0)(n_2 - \tilde{n}_2), \quad (25)$$

where we have used the fact that we may rewrite $E_{\mathbf{n}} = N\gamma_0 + (\gamma_1 - \gamma_0)n_1 + (\gamma_2 - \gamma_0)n_2$. In three dimensions there exist certain fluxes ϕ for which the spectrum becomes equidistant or quasiequidistant, i.e., there then exist a few energies characterizing the involved timescales. This is opposed to some general ϕ which reproduces a whole range of different timescales.

From the expression (25) we see that the energy spectrum becomes quasiequidistant whenever

$$\frac{\gamma_0 - \gamma_1}{\gamma_1 - \gamma_2} = q, \quad q \in \mathbb{Q}. \quad (26)$$

Writing $q = \frac{j}{j'}$ with $j, j' \in \mathbb{N}$, we find that given the solutions for γ_k in (23), Eq. (26) can be written as

$$\begin{aligned} j' \left[\sqrt{3} \cos \left(\frac{\phi}{3} \right) - \sin \left(\frac{\phi}{3} \right) \right] \\ = j \left[\sqrt{3} \cos \left(\frac{\phi}{3} \right) + \sin \left(\frac{\phi}{3} \right) \right]. \end{aligned} \quad (27)$$

As all three single-boson energies are continuous functions of ϕ , so are $(\gamma_0 - \gamma_1)$ and $(\gamma_1 - \gamma_2)$, and furthermore, except for the singularity when $\gamma_1 = \gamma_2$, which happens at $\phi = 0$, also the fraction (26) is a continuous function of ϕ . Disregarding this singularity, as $N \rightarrow \infty$ there will be infinitely many ϕ_j 's that fulfill the condition above; see Figs. 6(a) and 6(b). The spectrum at these ‘‘quasiequidistant points’’ becomes highly degenerate, but it is only perfectly equidistant for one of them, $\phi_1 = \pi/2$. This is the reason why for the other of these points we call the spectrum quasiequidistant, since here there exists more than a single energy difference. For a given ϕ_j , the energy differences between the nearby energies can be ordered $\Delta_j, 2\Delta_j, 3\Delta_j, \dots, j\Delta_j$. Note that the basic energy difference Δ_j is different for the various equidistant points. Solving (26) for ϕ_j leads to the following condition:

$$\tan \left(\frac{\phi_j}{3} \right) = \frac{\sqrt{3}}{2j+1}, \quad j \in \mathbb{N}, \quad (28)$$

which we have reached using (27), and introducing a new pair $n, n' \in \mathbb{N}$ where $j + j' = n'$ and $j' - j = n$. As this holds for any q , we may choose $n = 1$, which implies that $n' = 2j + 1$ and it leads to the expression above.

The equidistant points given by Eq. (28) become denser as the values of j increase, which manifests as a fractal structure

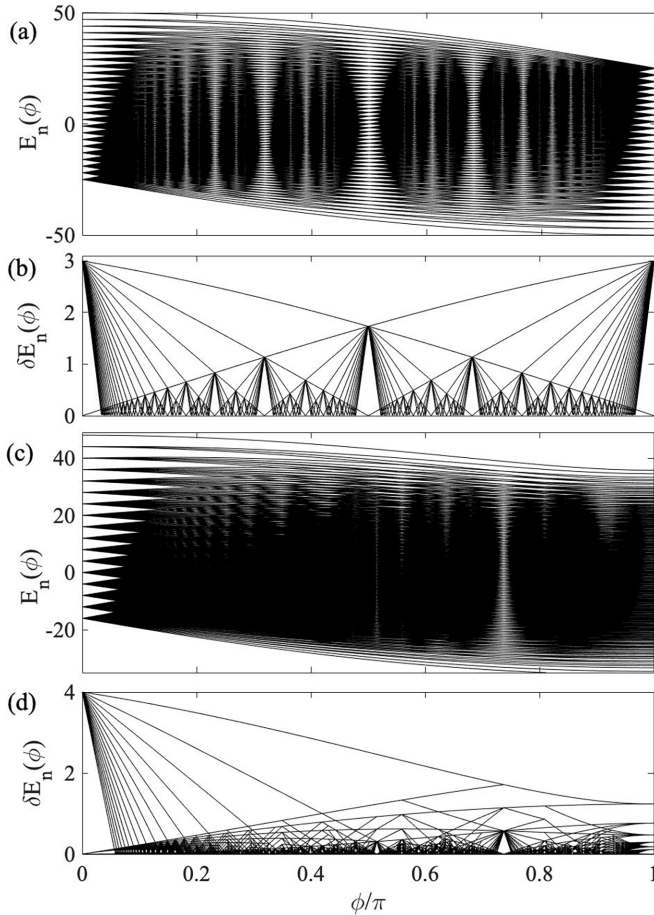


FIG. 6. The upper two plots, (a) and (b), show the spectra and the distances between nearby energies as a function of the flux ϕ , for the three-mode model with $N = 25$ bosons, while the lower two plots, (c) and (d), give the same for the four-mode case with $N = 16$. The fractal structure of the three-mode case is evident, while the four-mode spectrum does not display the same fractal properties.

of the spectrum; see Fig. 6, showing both the spectrum (a) and its nearby energy differences δE_n (b). The results of the energy differences demonstrate the concept of the equidistant points. As we will demonstrate in the next section, picking ϕ according to one of these points will result in novel dynamics.

D. The four-mode and higher-mode models

To fractal structure of the spectrum is rooted in the existence of special fluxes fulfilling the condition (26). The 3×3 matrix h gives three energies, and hence two energy differences, and the single condition derived from comparing these two. For the four-mode model (21) we find four eigenvalues γ_k (with $k = 1, 2, 3, 4$) of the corresponding matrix h . Following the same argument that led to the condition (26), for the four-mode model we are left with three conditions,

$$\frac{\gamma_3 - \gamma_0}{\gamma_2 - \gamma_0} = q_1, \quad \frac{\gamma_3 - \gamma_0}{\gamma_1 - \gamma_0} = q_2, \quad \frac{\gamma_2 - \gamma_0}{\gamma_1 - \gamma_0} = q_3, \quad (29)$$

where q_1, q_2 , and q_3 are all rational numbers. We can generalize this to a K -mode model in which the number of conditions becomes $(K - 1)(K - 2)/2$. It should be clear that it becomes

harder and harder, the larger K is, to find fluxes ϕ_j fulfilling all conditions simultaneously. As long as the conditions cannot be met for single fluxes, the spectrum cannot be fractal as for the three-mode model. We demonstrate this by displaying the spectrum and energy difference δE_n for the four-mode model in Figs. 6(c) and 6(d). It is possible, however, to find fractal spectra also for higher-mode models (four and six modes), as discussed next.

1. Ring models

The models defined via Eq. (21) are “fully connected,” i.e., each mode can exchange excitations with every other mode. It is, in principle, possible to introduce selections among the various tunneling processes, and hence block some of them. This motivates us to consider bosonic chains with periodic boundary conditions,

$$\hat{H} = \sum_{i=1}^K \hat{a}_i^\dagger \hat{a}_{i+1} e^{i\phi/K} + \text{H.c.}, \quad (30)$$

where $\hat{a}_{K+1} = \hat{a}_1$. Since we impose periodic boundary conditions, and the lattice has a ring structure, the phase ϕ becomes nontrivial because we cannot gauge it away. In the boson chain, it mimics a magnetic flux through the lattice ring. The FSL takes the form of a tetrahedron lattice for the fully connected four-mode case. When we consider instead the four-mode ring model, some of the links between sites in the tetrahedron lattice are cut; the number of sites each site couples to goes from twelve to eight. The resulting FSL has a rhombic structure, i.e., any 2D lattice plane forms a rhombic lattice. The characteristic equation for the corresponding matrix h becomes $\gamma^4 - 4\gamma^2 + 4\sin^2(\frac{\phi}{2}) = 0$, and the four eigenvalues (roots) can be expressed as

$$\gamma_{k\pm} = \pm \cos\left(\frac{\phi + \pi \times k}{2}\right), \quad k \in \{0, 1\}. \quad (31)$$

This leads to the following condition for the flux: $\phi = 2 \arctan(q)$ with $q \in \mathcal{Q}$. Similarly, for the six-mode ring model we find the eigenvalues

$$\gamma_k = \pm 2 \cos\left(\frac{\phi + 2\pi \times k}{6}\right) \quad k \in \{0, 1, 2\}, \quad (32)$$

giving the following condition for the quasiequidistant points: $\phi = 6 \arctan(\frac{q}{\sqrt{3}})$. In Fig. 7 we present the spectra and energy differences for the two ring models. Clearly, the two models’ spectra display a similar fractal structure to that for the three-mode model of Figs. 6(a) and 6(b). Interestingly, the three-mode model is also a ring model, just like those of Fig. 7. However, we have numerically verified that the five- and eight-mode models do not reproduce fractal spectra, i.e., they are not a property of ring-type coupling. We have noticed, though, that the spectrum $E_n(\phi)$ is symmetric around $E = 0$ for all fluxes ϕ whenever one considers an even number of boson modes. This suggest an additional chiral symmetry that holds only for ring models with an even number of modes.

V. EVOLUTION OF INITIALLY LOCALIZED STATES IN THE THREE-MODE BOSON MODEL

To further study manifestations of the fractal spectrum, we turn to study the evolution over time. While our focus

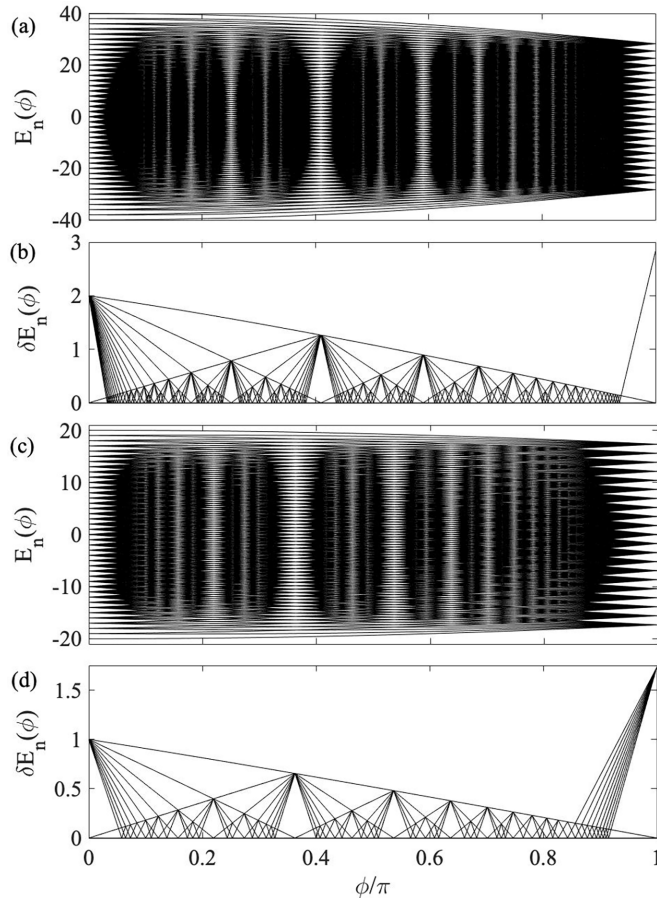


FIG. 7. The same as Fig. 6, but for the four-mode [upper two plots (a) and (b)] and six-mode [lower two plots (c) and (d)] ring models. The number of bosons is $N = 20$ and 10 for the two cases, respectively. By disregarding some of the terms in the Hamiltonian (21) to obtain the ring Hamiltonian (30), the number of conditions for having a quasiequidistant spectrum is reduced and it is possible to fulfill them simultaneously, leading to the reappearance of fractal spectra for these two models.

is on the three-mode case, let us start with a remark on the two-mode model, which produces a 1D FSL with tunneling rates $t\sqrt{(n+1)(N-n)}$. While a Bogoliubov transformation easily diagonalizes the Hamiltonian, we use the Schwinger spin-boson mapping instead. Here we identify a spin operator $\hat{S}_x = \frac{1}{2}(\hat{a}^\dagger \hat{b} + \hat{b}^\dagger \hat{a})$, such that the Hamiltonian is $\hat{H}_{\text{int}} = 2\hat{S}_x$, with the total spin $S = N/2$. The spectrum is equidistant, and any state returns to its initial state after the revival time $T_R = 2\pi$. This model was studied by Christandl *et al.* in terms of perfect state transfer in 1D chains with spatially varying tunneling rates [21], e.g., after half the revival time $T_R/2$ any initial state at one end of the chain will have traversed the chain to populate the other end. Recently, the model was experimentally explored with the particular Hamiltonian realized by coupling two photonic modes via a beam splitter [3]. To see the effect of the flux ϕ , we need to go up by one dimension.

As a demonstrating example, we consider a system of $N = 15$ bosons. Hence, the Fock states have a form $|n_a, n_b, n_c\rangle$, where $n_i \in \mathbb{N}$ and $n_a + n_b + n_c = 15$. $N = 15$ results in $\mathcal{S} =$

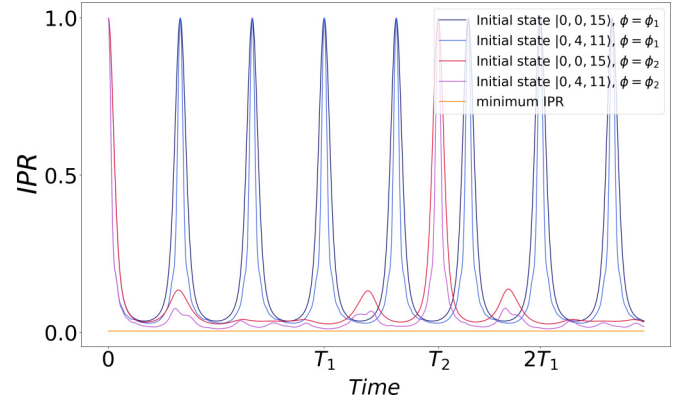


FIG. 8. The IPR for two different initial states and two different fluxes corresponding to equidistant points. The states display perfect revivals for both fluxes, even though the revival times differ between the fluxes (but not between the states). As a comparison, we also give the minimum possible IPR (yellow line). How the IPR is defined makes it easy to get fooled that a small value implies an extended distribution. The distributions remain fairly localized throughout; see Fig. 10.

136 different Fock states that make up the corresponding FSL. We shall look at the evolution of the two different initial states, taken to be $|15, 0, 0\rangle$ and $|11, 4, 0\rangle$, which are both initially completely localized on a single site somewhere in the FSL. To characterize the extent of the states, we consider the inverse partition ratio

$$\text{IPR}(t) = \sum_{\mathbf{n}} |\langle \mathbf{n} | \psi(t) \rangle|^4, \quad (33)$$

which gives the degree of localization in the FSL. For a fully localized state $\text{IPR} = 1$, while for a maximally delocalized one $\text{IPR} = 1/\mathcal{S}$, where \mathcal{S} is, as before, the number of sites of the FSL. When it comes to the choice of fluxes, we shall consider the time-evolution for the fluxes ϕ_1 and ϕ_2 according to Eq. (28). In addition, we pick a phase that does not coincide with any equidistant point, namely $\tilde{\phi} = \pi/100$.

The numerically extracted IPRs are depicted in Fig. 8. When the flux is one of the ϕ_j values, we see perfect recurrences of the IPR to its initial value $\text{IPR} = 1$. However, the state has not necessarily returned to its initial state in these instances, but it might have completely localized on another lattice site, as seen below. The state is spread over several lattice sites in between being completely localized. However, the IPR never drops close to its minimum value (a small IPR can still represent a localized distribution since it scales as $1/\text{occupied sites}$). Hence, even in-between the maximum localization, the distribution remains fairly localized in the lattice; see Fig. 10. For $\tilde{\phi}$ (not shown in the figure), when the spectrum is not quasiequidistant, we see no clear indicators of localization, even though the state is far from populating the whole lattice.

Recall that the constraint stemming from particle conservation removes one degree-of-freedom, which ensures, for example, that the participation vector $\vec{n}(\phi, t) = (n_a(\phi, t), n_b(\phi, t), n_c(\phi, t))$, with $n_i(\phi, t) = \langle \hat{n}_i \rangle$, lives in a 2D plane, i.e., the FSL. Thus, the trajectory gives us an idea of how the full distributions move around in the lattice, even

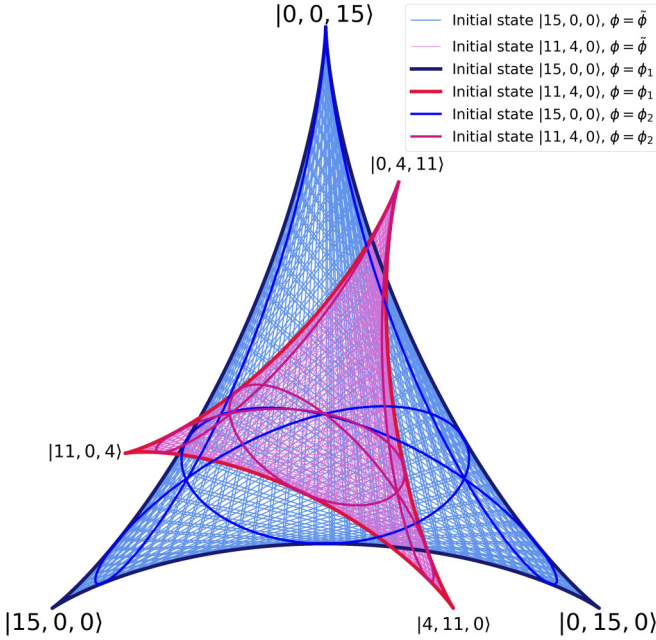


FIG. 9. Examples of the evolution of the occupation vector $\vec{n}(t) = (n_a(t), n_b(t), n_c(t))$, with $n_i(t) = \langle \hat{n}_i \rangle$ in the FSL for the three-mode model. The initial states are $|0, 0, 15\rangle$ (blue curves) and $|0, 4, 11\rangle$ (red curves), and the fluxes for the different curves are given in the inset. Note how the trajectories close whenever the flux is chosen as one of the equidistant points (signaling perfect revivals), while this is no longer true for a general flux (thin curves). In addition, the trajectories are found to be “shape invariant,” by which we mean that the two different initial states result in the same type of trajectories only rotated and scaled in size.

though it only captures the mean occupation but no higher moments of the distribution. In Fig. 9 we show examples of such trajectories for the same initial states and parameters as those used for Fig. 8. The first thing to notice is how the trajectory $\vec{n}(\phi_1, t)$ sets an outer boundary for all the other trajectories.

As pointed out, when ϕ_j agrees with one of the equidistant points, we encounter perfect revivals at times

$$T_j = \frac{2\pi}{\Delta_j}, \quad (34)$$

where Δ_j is the aforementioned smallest energy splitting for a given ϕ_j . The revivals manifest as closed trajectories of $\vec{n}(t)$ in the FSL. These loops form a symmetric pattern in the FSL, and the number of full 360° turns it makes before closing upon itself is found to be $2j - 1$. Thus, for $j = 1$ (i.e., $\phi_1 = \pi/2$), the distribution makes a single loop around the lattice, which is found to follow the lattice edges closely, i.e., there always remains a large population imbalance among the three modes. For ϕ_2 , the distribution makes three loops before returning to its initial states. For a flux away from any ϕ_j , we do not encounter such revivals, hence no closing of the trajectories. For the closed loops, there are “clustering points” in which many trajectories cross, the lattice origin being the most noticeable. A closer look reveals that for any initial Fock state, the resulting trajectories pass the origin [i.e., $n_a(t) = n_b(t) = n_c(t) = N/3$] for all ϕ_j with $j = 2, 3, 5, 6, 8, 9, \dots$

. Upon comparing the trajectories originating from the two different initial Fock states, $|0, 0, 15\rangle$ versus $|0, 4, 11\rangle$, we find that the shape and structure remain intact, however they are rotated and contracted. In Appendix we derive semiclassical equations of motion that exactly reproduce the trajectories.

The trajectories of Fig. 9 give the mean positions of the Fock-state distribution

$$P(\mathbf{n}, t) = |\langle \mathbf{n} | \psi(t) \rangle|^2. \quad (35)$$

However, they say nothing about its actual shape. In Fig. 10, by plotting the distribution $P(\mathbf{n}, t)$ at different times for the case of $\phi_1 = \pi/2$, it is seen that it remains fairly localized along the edges of the FSL. Furthermore, it propagates counterclockwise around the lattice, reflecting the breaking of time inversion as soon as the flux is nonzero (a zero flux does not produce a favored direction for the propagating distribution). The propagation is reminiscent of a Hall current; a perpendicular magnetic field applied to a 2D electronic gas implies a current living on the edge of the system. We consider a staggered magnetic field and notice that the direction of the current can be reversed by flipping the sign of the fluxes.

VI. TOWARDS THE SSH MODEL— AND THE APPEARANCE OF EDGE STATES

Speculating whether an underlying topological structure causes the edge currents seen in Fig. 10 is intriguing. A more thorough discussion regarding this topic for the FSLs can be found in Refs. [3,9]. Since translational invariance is absent, we encounter discrete energies rather than bands. However, it is interesting to note that for the chiral case with $\phi_1 = \pi/2$, we find $Z = N/2 + 1$ or $Z = N/2 + 1/2$ degenerate $E = 0$ energies for even and odd particle numbers N , respectively. These are not unique for the FSL but also appear for the translationally invariant lattice with a staggered field. In other words, the degenerate $E = 0$ energies in the FSL are the counterpart of a flat band.

Instead of exploring the properties of these $E = 0$ states for the three-mode model, let us introduce another model also supporting $E = 0$ eigenstates which are found to be living on the edge of the FSL. To construct a finite 1D FSL, we do not use a boson mode, but rather a spin- S subsystem via the mapping

$$\begin{aligned} (\hat{a}^\dagger + \hat{a}) &\rightarrow \hat{S}_x, \\ i(\hat{a}^\dagger - \hat{a}) &\rightarrow \hat{S}_y, \\ \hat{a}^\dagger \hat{a} &\rightarrow \hat{S}_z, \end{aligned} \quad (36)$$

where the \hat{S}^α 's are the SU(2) spin operators for a spin- S particle. Contrary to the case of a boson mode, this introduces both an upper and a lower bound/edge for the lattice. When this is applied to the JC model, one obtains a so-called central spin model—which is a model in which a central spin-1/2 particle interacts identically with N noninteracting spin-1/2 particles which form the large spin- S (i.e., $S = N/2$). The central spin model has served as a toy model for studying quantum criticality, as well as for analyzing non-Markovian decay of a qubit [22]. To achieve the desired FSL, we consider

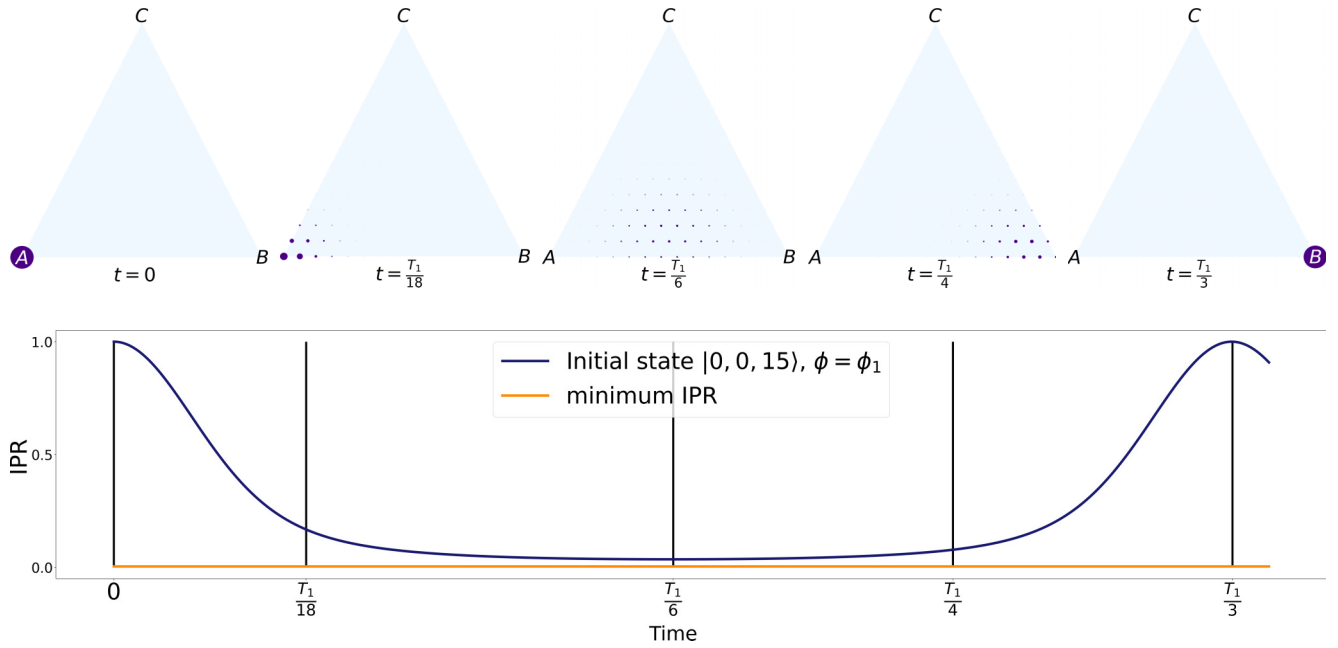


FIG. 10. The upper light blue triangles display snapshots of the Fock-state distributions (35) for the initial state $A = |0, 0, 15\rangle$ and for the flux $\phi_1 = \pi/2$. Initially the distribution occupies a single corner site, and after $T_R/3$ it has been transferred to another corner site. In between it stays well localized and traverses along the lower edge of the lattice. The lower plot gives the corresponding IPR (33), with the vertical lines indicating the time instances used for the distribution snapshots. Note that for the center distribution at $T_1/6$ we have $\text{IPR} \ll 1$, but still the distribution is well localized according to the upper figure.

the central spin model of the form

$$\begin{aligned} \hat{H}_{\text{int}}^{\text{CS}} &= g_x \hat{\sigma}^x \hat{S}^x + g_y \hat{\sigma}^y \hat{S}^y \\ &= g_+ (\hat{\sigma}^+ \hat{S}^- + \hat{\sigma}^- \hat{S}^+) + g_- (\hat{\sigma}^+ \hat{S}^+ + \hat{\sigma}^- \hat{S}^-), \end{aligned} \quad (37)$$

where $g_{\pm} = g_x \pm g_y$. This is the spin analog of the anisotropic quantum Rabi model (11), i.e., the two types of interaction terms couple with different strengths; for $g_x = g_y$ we regain a JC-type interaction, and for $g_y = 0$ we instead get a quantum Rabi-type interaction. As for the quantum Rabi model, the central spin model supports a \mathbb{Z}_2 -parity symmetry for general couplings g_x and g_y . This results in two decoupled 1D chains, one for each parity. Furthermore, the chains have lengths $2S + 1$, and provided $g_+ \neq g_-$ and $g_+, g_- \neq 0$, the tunneling rates will alternate between neighboring sites [see Fig. 11(a)], similar to that of the SSH model [16]. As for the SSH model, one finds for the central spin model two $E = 0$ eigenstates that become exponentially localized at either of the edges. More precisely, the probability to populate site i for such a state scales as $P_i \propto (\frac{g_{\pm}}{g_{\mp}})^{S-i}$. Each localized state belongs to either of the two parity sectors, and in Fig. 11(b) we show one of them for $g_+ = 0.9g_-$. For the two-mode JC model on resonance, one also finds localized edge states [9], but unlike those of the central spin model, these are not exponentially localized.

VII. EXAMPLES OF FOCK-STATE LATTICES

In quantum optics, one encounters a range of models, comprising a few degrees-of-freedom, that describe the interaction between quantized light and matter. Many of these are extensions and generalizations of the JC model toward multimode

and multilevel atoms [12]. They often generate interesting FSLs with known, translationally invariant counterparts in condensed-matter physics. In Table I, several models are listed, along with their respective interaction Hamiltonians, and with information about how the relevant FSL looks. Below, we discuss a few of these models.

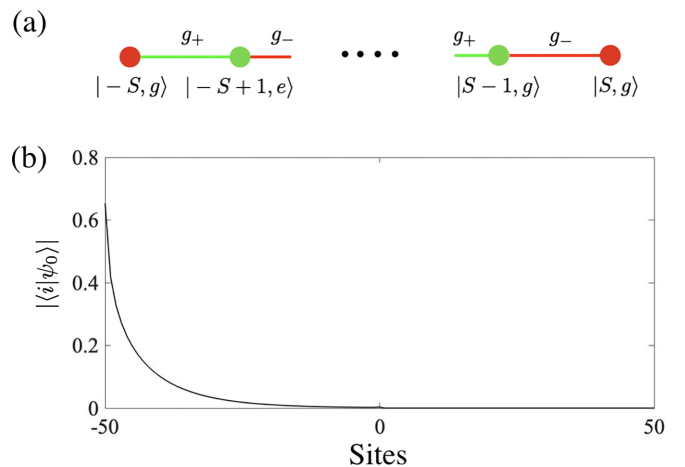


FIG. 11. The FSL (a) emerging from the central spin model (37) with anisotropic coupling amplitudes g_{\pm} . The red (green) dots mark Fock states with spin-1/2 in the $|g\rangle$ ($|e\rangle$) states, respectively. The parity symmetry of the model implies a similar FSL but belonging to the other parity sector with the green (red) dots swapped. In (b) we show the exponentially localized $E = 0$ energy eigenstate $|\psi_0\rangle$ in a 101-site lattice with $g_+/g_- = 0.9$. In the other parity sector, there is an equivalent edge state localized to the right edge instead.

TABLE I. A collection of atom-light interaction Hamiltonians and their corresponding FSLs. Many of these appear frequently in the quantum optics community. Some of them we have discussed in some detail in the main text, e.g., the two-mode and three-mode JC models. $\hat{\sigma}_{ij} = |i\rangle\langle j| + |j\rangle\langle i|$.

Model	Interaction Hamiltonian	Lattice type
Jaynes-Cummings	$\hat{H}_{\text{int}} = g(\hat{a}^\dagger \hat{\sigma}_- + \hat{a} \hat{\sigma}_+)$	Double-well, Fig. 4(a)
Quantum Rabi	$\hat{H}_{\text{int}} = g(\hat{a}^\dagger + \hat{a}) \hat{\sigma}_x$	1D chain, Fig. 4(b)
Anisotropic quantum Rabi	$\hat{H}_{\text{int}} = g_{\text{jc}}(\hat{\sigma}_+ \hat{a} + \hat{a}^\dagger \hat{\sigma}_-) + g_{\text{ajc}}(\hat{\sigma}_- \hat{a} + \hat{a}^\dagger \hat{\sigma}_+)$	Infinite SSH chain
N -atom Dicke	$\hat{H}_{\text{int}} = g(\hat{a}^\dagger + \hat{a}) \hat{S}_x$	Square lattice
N atom Tavis-Cummings	$\hat{H}_{\text{int}} = g(\hat{a}^\dagger \hat{S}_- + \hat{a} \hat{S}_+)$	N potential-well
Central spin model	$\hat{H}_{\text{int}} = g_x \hat{\sigma}_x \hat{S}_x + g_y \hat{\sigma}_y \hat{S}_y$	Finite SSH chain, Fig. 11(a)
Driven quantum Rabi	$\hat{H}_{\text{int}} = g(\hat{a}^\dagger + \hat{a}) \hat{\sigma}_x + \eta(\hat{a}^\dagger + \hat{a})$	Creutz ladder, Fig. 4(d)
Single mode Λ	$\hat{H}_{\text{int}} = g(\hat{a}^\dagger + \hat{a})(\hat{\lambda}^{(1)} + \hat{\lambda}^{(6)})$	Lieb ladder
Two-mode JC	$\hat{H}_{\text{int}} = g_a(\hat{a}^\dagger \hat{\sigma}_- + \hat{a} \hat{\sigma}_+) + g_b(\hat{b}^\dagger \hat{\sigma}_- + \hat{b} \hat{\sigma}_+)$	SSH chain
Two-mode detuned JC	$\hat{H}_{\text{int}} = t(\hat{a}^\dagger \hat{b} + \hat{b}^\dagger \hat{a})$	CDEL chain
Two-mode quantum Rabi	$\hat{H}_{\text{int}} = g[(\hat{a}^\dagger + \hat{a}) + (\hat{b}^\dagger + \hat{b})] \hat{\sigma}_x$	(Layered) square lattice
Two mode Λ	$\hat{H}_{\text{int}} = g_a(\hat{a}^\dagger + \hat{a}) \hat{\sigma}_{12} + g_b(\hat{b}^\dagger + \hat{b}) \hat{\sigma}_{23}$	2D Lieb lattice
Three-mode JC	$\hat{H}_{\text{int}} = g_a(\hat{a}^\dagger \hat{\sigma}_- + \hat{a} \hat{\sigma}_+) + g_b(\hat{b}^\dagger \hat{\sigma}_- + \hat{b} \hat{\sigma}_+) + g_c(\hat{c}^\dagger \hat{\sigma}_- + \hat{c} \hat{\sigma}_+)$	Hexagonal lattice
Three-mode detuned JC	$\hat{H}_{\text{int}} = t(\hat{a}^\dagger \hat{b} e^{i\varphi} + \hat{b}^\dagger \hat{c} + \hat{a}^\dagger \hat{c} + \text{H.c.})$	Triangular lattice, Fig. 5
Three-mode tripod	$\hat{H}_{\text{int}} = g_a(\hat{a}^\dagger + \hat{a}) \hat{\sigma}_{12} + g_b(\hat{b}^\dagger + \hat{b}) \hat{\sigma}_{13} + g_c(\hat{c}^\dagger + \hat{c}) \hat{\sigma}_{14}$	Perovskite lattice
Three-mode quantum Rabi	$\hat{H}_{\text{int}} = g[(\hat{a}^\dagger + \hat{a}) + (\hat{b}^\dagger + \hat{b}) + (\hat{c}^\dagger + \hat{c})] \hat{\sigma}_x$	Cubic lattice
Four-mode detuned JC1	$\hat{H}_{\text{int}} = t \sum_{j,i=1}^4 e^{i\phi_{ij}} \hat{a}_i^\dagger \hat{a}_j$	Tetrahedral lattice
Four-mode detuned JC2	$\hat{H}_{\text{int}} = t \sum_{i=1}^4 e^{i\phi_i} \hat{a}_i^\dagger \hat{a}_{i+1} + \text{H.c.}$	Rhombic 3D lattice

(i) *Driven quantum Rabi model.* The FSL belonging to the quantum Rabi model was shown in Fig. 4(b), where the \mathbb{Z}_2 -parity symmetry splits the lattice into two 1D chains, one for each parity. We may break this parity by including a driving term, which induces tunneling along the legs of the FSL ladder, as depicted in Fig. 4(d). This lattice is a special type of a Creutz ladder [17]. The more standard Creutz ladder appears if we also include an atomic driving term that results in nonzero tunneling terms along the rungs of the ladder. In the Creutz ladder, we have competing nearest- and next-nearest-neighbor tunneling terms. A property of the Creutz ladder lattice is the presence of a dispersionless flat band when the tunneling rates are properly tuned. For our model, if we rotate the spin, $\hat{\sigma}_x \rightarrow \hat{\sigma}_z$, the Hamiltonian takes the simple form $\hat{H}_{\text{int}} = (\eta \pm g)(\hat{a}^\dagger + \hat{a})$. For $g = \eta$, i.e., the same amplitude of the tunneling rates, we find an infinite number of degenerate $E = 0$ eigenstates. These are the corresponding flat band of the Creutz ladder, now manifested in the FSL.

(ii) *Two-mode Λ model.* The Lieb lattice is another paradigm model hosting a flat band. In 2D, it is a ‘‘punctured’’ squared lattice where every fourth lattice point has been excluded. The unit cell now contains three sites, with two having nonzero tunneling elements to two neighbors and the third site couples to four neighbors. The lattice geometry provides a destructive interference mechanism that may completely hinder mobility, resulting in an $E = 0$ flat band in the tight-binding limit [23]. The remaining two bands touch in a Dirac cone in the center of the Brillouin zone. We can achieve this lattice type in a system of a three-level Λ atom (two lower states and one excited), with the transition of each arm of the atom coupled to different boson modes. One finds that the destructive interference also survives in the FSL, and one thereby derives an infinite number of degenerate $E = 0$ eigenstates.

(iii) *Three-mode tripod model.* The generalization of the three-level Λ atom to four levels consists in adding one more arm, which is called the tripod atom. We can then couple each arm of the tripod to an individual mode such that we have a three-mode model. The resulting 3D lattice bears similarities with the Lieb lattice, i.e., it is a punctured cubic lattice with a unit cell containing four points. The translationally invariant version is called a perovskite-type lattice, and as for the Lieb lattice, it supports bands with nontrivial topology, i.e., their Chern numbers are nonzero [24]. The flat bands in the two-mode Λ and three-mode tripod systems are related to dark states in these models, i.e., $E = 0$ eigenstates.

The list of Table I is by no means complete. As one sees in Ref. [9], many topological features of translationally invariant lattices survive in FSLs with the same geometry. Topological invariants, like the Chern number, are not directly applicable for FSLs, and instead, alternative topological numbers are studied [9]. Hence, given one favorite lattice with some interesting properties, e.g., nontrivial topology, one can work backward and ask for some interaction Hamiltonian that generates the corresponding FSL. For example, bilayered lattices may possess novel properties, such as bilayered Lieb lattices that can produce high Chern numbers. It is often straightforward to introduce more layers in the FSL by including additional internal atomic levels.

VIII. CONCLUDING REMARKS

In this work, we have taken an alternative approach to analyze various spin-boson models known from quantum optics. This idea of relying on FSLs was first brought up in [8] and later extended in [9]. In these works, the focus was on the multimode JC model. Part of the present work explores the same models, and we find a set of new properties. The spectra

for the three-mode boson model, when a synthetic magnetic flux has been added, are found to be fractal, akin to the Hofstadter butterfly. The flux of the FSL is, however, staggered rather than uniform (a uniform flux would not render a fractal spectrum for the triangular FSL). The fractal structure cannot be explained by the same arguments used for the Hofstadter butterfly, as this relies on varying sizes of the lattice's unit cell. Instead, the emergence of our fractal structure is understood in terms of specific fluxes ϕ_j that cause a high degeneracy in the spectrum. The fractal structure is generally lost for a higher number of boson modes, but it can be restored for the four- and six-mode cases provided one adds some selection among the tunneling terms between the modes.

The system's evolution depends very much on the flux, and at the quasiequidistant points ϕ_j , the system shows perfect revivals. In the FSL, given that we start in a Fock state, for these fluxes the distribution $P(\mathbf{n}, t)$ remains well localized and follows closed loops. Since the flux breaks time-reversal symmetry, the loops are traversed either clockwise or anti-clockwise depending on the sign of ϕ_j . One also finds that these closed trajectories have mirror symmetry with respect to the axis intersecting the lattice origin and the site where the state is initialized. Furthermore, the index j determines how many twists the distribution makes before it returns to the initial site. There is also an inherent scale invariance of these trajectories; for a given ϕ_j , the trajectories are identical in structure irrespective of the specific initial Fock state, i.e., they only differ in orientation and size.

We also demonstrated how fractal spectra appear in a four- and six-mode boson model. The FSL of the three-mode model is two-dimensional, and the occupation vector $\vec{n}(t)$ evolves in a plane defined by a fixed total boson number N . Likewise, we have a four-component occupation vector $\vec{n}(t)$ for the four-mode model, but the conserved particle number implies that it is projected into a 3D FSL. The properties of the corresponding trajectories, i.e., how the state evolves within the FSLs, were not considered, but we expect similar behavior to that for the three-mode model.

A boson degree-of-freedom results in infinite FSLs, unless some symmetry restricts it, e.g., particle conservation. Spin degrees-of-freedom have finite-size Hilbert spaces and thereby finite-size FSLs. We considered one such example, the anisotropic central spin model, and we showed how this model has a topological property manifested in $E = 0$ states exponentially localized to the edges of the lattice. Without going into any details, we listed other models and mentioned which type of FSLs they generate. One exciting example is systems with "flat bands" being a huge $E = 0$ degeneracy. Of course, one can consider other models beyond those mentioned in this paper. Note also that we use the Fock states, i.e., bare states, in order to construct the FSL. In short, the total Hamiltonian has the form $\hat{H} = \hat{H}_0 + \hat{H}_{\text{int}}$, where the Fock states are the eigenstates of \hat{H}_0 , and \hat{H}_{int} constitute the FSL. We could generalize this to a situation in which \hat{H}_0 is not diagonal in the Fock basis but instead in another (dressed) basis, such as the driven JC model, $\hat{H} = \hat{H}_{\text{JC}} + \eta(\hat{a}^\dagger + \hat{a})$, and we could consider the JC dressed states rather than the bare Fock states. The drive term will then constitute a new state-space lattice (dressed state lattice), which becomes a 1D chain in this example. As another example, the quantum Rabi

model could be written as $\hat{H}_{\text{R}} = \hat{H}_{\text{JC}} + g(\hat{a}^\dagger \hat{\sigma}^+ + \hat{a} \hat{\sigma}^-)$, such that it is expressed as a JC Hamiltonian plus the counter-rotating terms [12]. In the JC dressed state basis, the resulting state space lattice formed by the counter-rotating terms will be two decoupled 1D parity chains. Naturally, experimentally the bare Fock states are typically more relevant from a perspective of detection. However, we mention this to stress the greater flexibility of the method by allowing for other bases.

ACKNOWLEDGMENTS

The authors thank Themistoklis Mavrogordatos for helpful feedback on the manuscript. We acknowledge financial support from VR-Vetenskapsrådet (The Swedish Research Council) and KAW (The Knut and Alice Wallenberg Foundation).

APPENDIX: EQUATIONS OF MOTION FOR THE MEAN VALUES OF THE THREE-MODE BOSON MODEL

The multimode bosonic model (21) is quadratic and thereby solvable via a Bogoliubov transformation. Moreover, as a quadratic model it follows that an initial Gaussian state, e.g., any coherent or squeezed states, remains Gaussian at all times. Thus, a Gaussian quantum phase space distribution remains localized and follows the classical phase-space trajectories. It is convenient to work with the classical canonical variables for position

$$\hat{x} = \frac{(\hat{a}^\dagger + \hat{a})}{\sqrt{2}} \quad (\text{A1})$$

and momentum

$$\hat{p}_x = \frac{(\hat{a}^\dagger - \hat{a})}{\sqrt{2}}. \quad (\text{A2})$$

Using the fact that the Heisenberg and Hamilton equations have the same structure for a quadratic bosonic Hamiltonian, for the three-mode case we get the equations of motion

$$\begin{aligned} \dot{x}_a &= -p_b - p_c, \\ \dot{x}_b &= -p_a - \cos(\varphi)p_c - \sin(\varphi)x_c, \\ \dot{x}_c &= -p_a - \cos(\varphi)p_b + \sin(\varphi)x_b, \end{aligned} \quad (\text{A3})$$

and

$$\begin{aligned} \dot{p}_a &= x_b + x_c, \\ \dot{p}_b &= x_a + \cos(\varphi)x_c - \sin(\varphi)p_c, \\ \dot{p}_c &= x_a + \cos(\varphi)x_b + \sin(\varphi)p_b, \end{aligned} \quad (\text{A4})$$

such that $\langle \hat{n}_\alpha \rangle_t = [p_\alpha^2(t) + x_\alpha^2(t)]/2$. Since a Gaussian state (apart from the vacuum) does not contain a fixed number of bosons N , this means for the FSLs that it will populate different triangular FSLs—one for each boson number N . However, the shape and structure of the trajectories in the FSLs are invariant for different N -values; the particle number only provides a scaling of the trajectories as demonstrated in Fig. 9.

For the above equations to reproduce the correct trajectories of Fig. 9, where the initial state is a Fock state $|N, 0, 0\rangle$,

one should use the initial conditions $(x_a, x_b, x_c, p_a, p_b, p_c) = (\sqrt{2N}, 0, 0, 0, 0, 0)$. We have numerically confirmed that

these trajectories agree with those obtained from diagonalizing the full N -boson Hamiltonian.

-
- [1] A. Altland and B. Simmons, *Condensed Matter Field Theory* (Cambridge University Press, Cambridge, 2010).
- [2] M. Lewenstein, A. Sanpera, V. Ahufinger, B. Damski, A. Sen(De), and U. Sen, *Adv. Phys.* **56**, 243 (2007); I. Bloch, J. Dalibard, and W. Zwerger, *Rev. Mod. Phys.* **80**, 885 (2008); P. Zoller and C. W. Gardiner, *The Quantum World Of Ultra-cold Atoms And Light—Book III: Ultra-cold Atoms* (World Scientific, Singapore, 2017).
- [3] T. J. Sturges, T. McDermott, A. Buraczewski, W. R. Clements, J. J. Renema, S. W. Nam, T. Gerrits, A. Lita, W. S. Kolthammer, A. Eckstein, I. A. Walmsley, and M. Stobiska, *npj Quantum Inf.* **7**, 91 (2021).
- [4] O. Boada, A. Celi, and J. I. Latorre, and M. Lewenstein, *Phys. Rev. Lett.* **108**, 133001 (2012).
- [5] H. M. Price, T. Ozawa, and N. Goldman, *Phys. Rev. A* **95**, 023607 (2017).
- [6] A. Perez-Leija, H. Moya-Cessa, A. Szameit, and D. N. Christodoulides, *Opt. Lett.* **35**, 2409 (2010).
- [7] K. Tschernig, R. de J. León-Montiel, A. Pérez-Leija, and K. Busch, *Photon. Res.* **8**, 1161 (2020).
- [8] D.-W. Wang, H. Cai, R.-B. Liu, and M. O. Scully, *Phys. Rev. Lett.* **116**, 220502 (2016).
- [9] H. Cai and D.-W. Wang, *Natl. Sci. Rev.* **8**, nwaa196 (2021).
- [10] D. R. Hofstadter, *Phys. Rev. B* **14**, 2239 (1976).
- [11] E. T. Jaynes and F. W. Cummings, *Comparison of Quantum and Semiclassical Radiation Theories with Application to the Beam Maser*, in Proceedings of the IEEE (IEEE, Piscataway, NJ, 1963), Vol. 51, no. 1, pp. 89–109.
- [12] J. Larson and T. Mavrogordatos, *The Jaynes-Cummings Model and Its Descendants* (IOP, Bristol, UK, 2022).
- [13] J. Larson, E. Sjöqvist, and P. Öhberg, *Conical Intersections in Physics* (Springer, Heidelberg, 2020).
- [14] J. Casanova, G. Romero, I. Lizuain, J. J. García-Ripoll, and E. Solano, *Phys. Rev. Lett.* **105**, 263603 (2010).
- [15] Q.-T. Xie, S. Cui, J.-P. Cao, L. Amico, and H. Fan, *Phys. Rev. X* **4**, 021046 (2014).
- [16] W. P. Su, J. R. Schrieffer, and A. J. Heeger, *Phys. Rev. Lett.* **42**, 1698 (1979).
- [17] M. Creutz, *Phys. Rev. Lett.* **83**, 2636 (1999).
- [18] C. Gardiner and P. Zoller, *Quantum Noise* (Springer, Heidelberg, 2004).
- [19] A. Nunnenkamp, J. Koch, and S. M. Girvin, *New J. Phys.* **13**, 095008 (2011).
- [20] One realization of a Hamiltonian generating a FSL with a constant (i.e., not staggered) flux through every plaquette is $\hat{H}_{\text{con}} = (e^{i\phi(\hat{n}_a + \hat{n}_c)} \hat{a}^\dagger \hat{b} + e^{i\phi} \hat{b}^\dagger \hat{c} + e^{i\phi(\hat{n}_a + \hat{n}_c)} \hat{c}^\dagger \hat{a}) + \text{H.c.}$
- [21] M. Christandl, N. Datta, A. Ekert, and A. J. Landahl, *Phys. Rev. Lett.* **92**, 187902 (2004).
- [22] N. D. Mermin, *Physica A* **177**, 561 (1991); H.-P. Breuer, D. Burgarth, and F. Petruccione, *Phys. Rev. B* **70**, 045323 (2004).
- [23] E. H. Lieb, *Phys. Rev. Lett.* **62**, 1201 (1989).
- [24] C. Weeks and M. Franz, *Phys. Rev. B* **82**, 085310 (2010).